PHYSICAL REVIEW B **109**, 235202 (2024)

Intrinsically ultralow lattice thermal conductivity and giant thermoelectric effect in Ag-based intercalated layered crystalline solids

Junpeng Yuan, Min Li, and Hui Wang *

School of Physics, Hunan Key Laboratory of Super Microstructure and Ultrafast Process,
Hunan Key Laboratory of Nanophotonics and Devices, State Key Laboratory of Powder Metallurgy,
Central South University, Changsha 410083, China

(Received 7 February 2024; revised 14 April 2024; accepted 9 May 2024; published 3 June 2024)

Understanding the nature of low thermal conductivity and phonon transport properties is critical for the design of potential thermoelectric materials. Based on density-functional theory combined with the phonon Peierls-Boltzmann transport equation, we reveal that Ag-based intercalated layered materials $\mathrm{AgBi}X_2$ ($X =$ S, Se, and Te) have inherently low lattice thermal conductivity, which is mainly attributed to the anticrossing behavior of low-frequency optical phonons and longitudinal acoustic phonons induced by the rattling mode of the cations. It is found that the optical phonons in $\mathrm{AgBiS_2}$ contribute dominantly (up to 65%) to the total thermal conductivity, originating from the weak bonding nature of intercalated Ag atoms that leads to strong anharmonicity and softening of transverse acoustic phonons. Electronic relaxation times under acoustic deformation potential scattering, polar optical phonon scattering, and ionized impurity scattering are considered to obtain reasonable electron transport properties. The *ZT* value of *p*-type $\mathrm{AgBiS_2}$ reaches 1.77 for optimal doping at room temperature, which can further be enhanced to ∼2.6 through strain engineering. The present work demonstrates that chemically controlled weak bonding in Ag-based intercalated layered structure produces intrinsically low thermal conductivity and provides important theoretical insight for thermal insulator and thermoelectric applications.

DOI: 10.1103/PhysRevB.109.235202

I. INTRODUCTION

Thermoelectric (TE) materials and devices are crucial for energy conversion and efficient utilization, as they can directly convert waste heat into electricity and vice versa [1]. High thermoelectric performance requires simultaneously high electrical transport properties and low thermal conductivity. In the equation of the dimensionless figure of merit: $ZT = S^2\sigma T/(\kappa_l + \kappa_e)$, the lattice thermal conductivity (κ_l) is the only independent parameter, while other parameters such as electronic thermal conductivity (κ_e), electrical conductivity (σ), and Seebeck coefficient (S) are entangled with each other [2,3]. Extrinsic strategies such as nanostructuring and alloying have been shown to strongly suppress lattice thermal conductivity, but it is inevitably detrimental to electrical mobility [4]. Therefore, it is crucial and indispensable to search for new materials with inherently low thermal conductivity that weakly couples to electric properties, so as to control electrical transport to induce high thermoelectric performance.

Rigorous investigations on minimal κ_l have revealed unconventional phonon-scattering mechanisms in certain TE crystalline solids, such as liquidlike thermal conduction in $\mathrm{AgCrSe_2}$ [5], thermal damping in $\mathrm{Cu_2Se}$ due to liquidlike atomic dynamics [6], and resonant phonon scattering in clathrates with randomly rattling atoms [7]. The intrinsically low κ_l in two-dimensional layered compounds such as SnSe [8], GeSe [9], and ScSI [10] originates from the different bonding environments between layers, coupled with anharmonicity caused by lone pairs. Other intrinsic phenomena that lead to low κ_l include ferroelectric instability, multicenter bonding, and resonant bonding [11,12]. It is worth noting that recent work reports that Cd-doped $\mathrm{AgSbTe_2}$ reduces the Anderson localization caused by disorder and local strain regulates phonon vibration coupling, giving rise to remarkably enhanced *ZT* up to 1.5 at room temperature [13]. Exploring the potential correlations between lattice dynamics, crystal structure, and chemical bonding is not only fundamental to understanding phonon transport but also sheds light on the design of new thermoelectric materials.

In this work, we investigate a family of silver ion intercalated layered crystalline solids $\mathrm{AgBi}X_2$ ($X =$ S, Se, and Te), in analogs to $M\mathrm{CrSe_2}$ ($M =$ Cu and Ag) [14,15]. Structural stability is demonstrated from mechanics, thermodynamics, and kinetics using first-principles calculations. By solving the linear phonon Boltzmann transport equation (BTE), our results indicate that $\mathrm{AgBi}X_2$ has low thermal conductivity ($\kappa_l < 1\mathrm{W/mK}$) due to the rattling mode of metal atoms. It is unexpectedly found that the optical phonon contribution to total κ_l in $\mathrm{AgBiS_2}$ is as high as 65%, which originates from the weak bonding between Ag atoms that dominate transverse acoustic phonons and S atoms that is responsible for the high-frequency optical phonon group. Combining three scattering mechanisms [16], it is found that *p*-type $\mathrm{AgBiS_2}$ exhibits promising electrical transport properties, with *ZT* of 1.77 for optimal carrier concentration at room temperature.

---

[*] Corresponding author: huiwang@csu.edu.cn

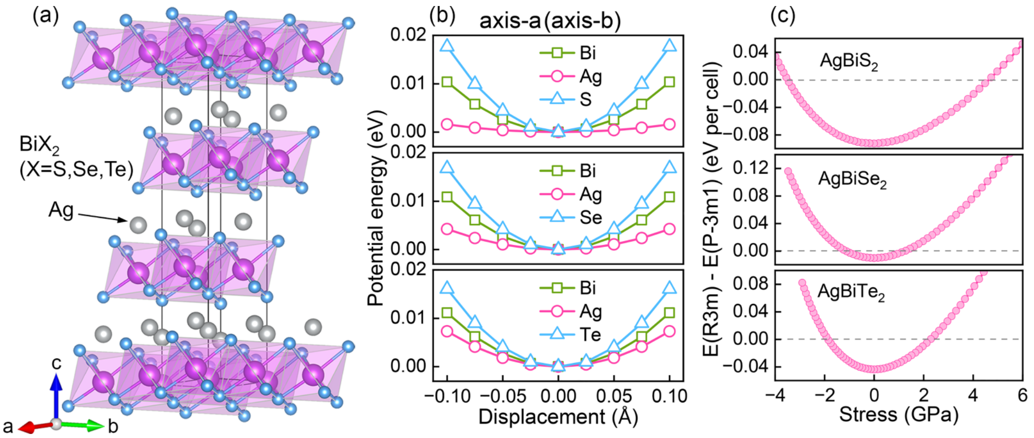

FIG. 1. (a) Crystal structure of AgBiX_2. (b) The potential energy of Bi, Ag, S, Se, and Te atoms in AgBiX_2 with respect to displacement along the *a*-axis (*b*-axis) direction. (c) Total energy barrier of AgBiX_2 in the *R*3m phase (Ag at tetrahedral interstitial sites) and *P*-3*m*1 phase (Ag at octahedral interstitial sites) as a function of hydrostatic stress.

Importantly, power factor σS^2 remains almost unchanged and κ_l can be further decreased through moderate strain engineering, eventually giving rise to giant *ZT* of ∼2.6. This work highlights the regulation of chemical bonding and the influence of external stimuli to trap low κ_l and elucidates the microscopic origin that provides guidelines for the design of thermal insulator and thermoelectric devices.

II. COMPUTATIONAL METHODS

First-principles calculations were performed using the Vienna *Ab initio* Simulation Package (VASP) with the projected augmented-wave method [17,18], where the Perdew-Burke-Ernzerhof functional of generalized gradient approximation was employed in exchange-correlation potential [19]. The kinetic energy cutoff of the plane-wave basis set was set to 500 eV [20,21] and the optimum structures of the three compounds were captured on an 11 × 11 × 11 *k*-point mesh. The energy convergence criterion for electron self-consistency was 10^{-8} eV, and the force convergence standard was less than 1 meV/Å [22,23].

The interatomic force constants are obtained using the supercell finite-displacement approach. A 4 × 4 × 4 supercell with a 2 × 2 × 2 *k*-point grid was implemented in the PHONOPY code [24] to calculate the second-order (harmonic) force constants while also obtaining the phonon dispersion curve and phonon density of states. The third-order force constant (anharmonic) was computed using a 3 × 3 × 3 supercell with a 1 × 1 × 1 *k*-point grid [25,26] where the force cutoff radius was set to the eighth-neighbor atomic distance. The lattice thermal conductivity κ_l was calculated by iteratively solving the linearized Peierls-Boltzmann transport equation as implemented in the SHENGBTE software [25,27]. A 15 × 15 × 15 *q* grid with a Gaussian smear parameter of 0.5 was used to ensure convergence of the results. *Ab initio* molecular dynamics (AIMD) 5000-step simulations were performed in the temperature range between 300 and 800 K, with the simulation time step set to 2 fs [28,29].

Electron transport properties, including Seebeck coefficient (*S*), electrical conductivity (σ), and electron/hole thermal conductivity (κ_e or k_h), were calculated using the AMSET package [16]. In order to obtain reliable carrier relaxation time, three scattering mechanisms were considered: acoustic deformation potential scattering (ADP), polar optical phonon scattering (POP), and ionized impurity scattering (IMP). The band structure, elastic constant (C_{ij}), static (ε_s) and high-frequency dielectric constant (ε_∞), and polar phonon frequency (ω_p) were required as input parameters (details are available in Supplemental Material, Tables S1–S4) [30]. The electron transport coefficient was accurately determined using a band interpolation factor of 15 [31].

III. RESULTS AND DISCUSSION

A. Structural stability and weak chemical bonds

AgBiX_2 is a rhombohedral crystal (having 4 atoms) with space group *R*3*m*. As shown in Fig. 1(a), Bi atoms and *X*-group atoms construct a sublattice (BiX_2) that is combined with intercalated silver atoms along the *c*-axis direction to form a bulk material. The *X* atoms are closely packed, forming a larger octahedral cage containing the Bi atoms and smaller tetrahedra surrounding the Ag atoms. The calculated primitive-cell lattice constant of $AgBiS_2$, $AgBiSe_2$, and $AgBiTe_2$ are 7.52, 7.81, and 8.19 Å, respectively. There are two local coordination bond lengths for Bi (octahedral) and Ag (tetrahedral) atoms (see Fig. S1). For the hexagonal conventional unit cell of AgBiX_2 (12 atoms), Bi octahedra and Ag tetrahedra form alternating chains in the *c*-axis direction.

Figure 1(b) shows the potential-energy surface of each atom in AgBiX_2 away from the equilibrium position along the in-plane direction (e.g., *a* axis). It is found that the Ag atoms are located in a shallow potential well. Particularly, the potential-energy surface of the Ag atoms in $AgBiS_2$ is very flat, indicating its weak bonding with adjacent atomic environment. Figure S2 further illustrates that tetrahedral Ag atoms easily move along the *a*/*b* axis plane. Additionally, the electron localization function (ELF) [32] was calculated to better understand the bonding characteristics. Figure S3 shows that very low ELF values (cyan) occur between Ag and X (S, Se, or Te) atoms. Likewise, low ELF values (green) are found between Bi and *X* (S, Se, or Te) atoms, implying ionic bonding. The elastic constants listed in Supplemental Material

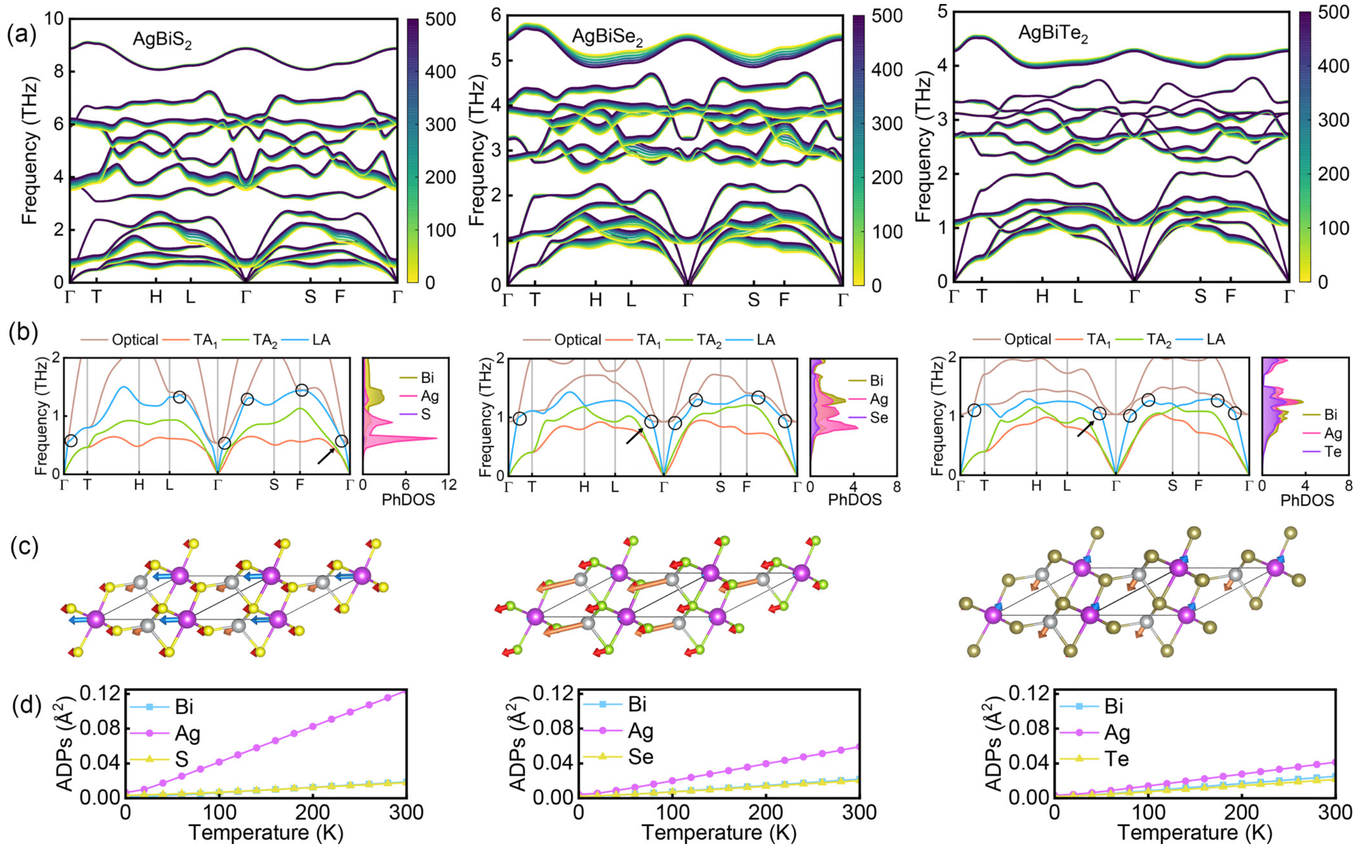

FIG. 2. (a) Phonon dispersion of AgBiX_2 at finite temperature. The color bar represents the temperature range. (b) Calculated phonon dispersion and atom-projected phonon density of states (PhDOS) for $AgBiS_2$, $AgBiSe_2$, and $AgBiTe_2$. The orange, green, and blue lines represent two transverse (TA_1, TA_2) and one longitudinal (LA) acoustic phonon modes. The brown line marks the optical phonon mode. (c) Atomic vibration modes of AgBiX_2 at the anticrossing point. The length of the arrow is proportional to the magnitude of the atomic displacement. (d) Atomic displacement parameters (ADPs) of different atoms along the a-axis direction in AgBiX_2.

[30], Table S1 meet the mechanical stability criterion [33] as shown in Eq. (1), indicating that AgBiX_2 (X = S, Se, or Te) are mechanically stable.

$$C_{11} - C_{12} > 0, \quad C_{13}^2 < 0.5C_{33}(C_{11} + C_{12}),$$
$$C_{14}^2 < 0.5C_{44}(C_{11} - C_{12}), \quad C_{44} > 0. \tag{1}$$

In addition, as the chalcogen atomic number increases, the mechanical parameters of these three compounds decrease, including shear modulus (G), bulk modulus (B), and Young's modulus (E), as shown in Table S1. One may note that Poisson's ratio (ν) is greater than 0.26 [34], suggesting that these three Ag-based compounds are ductile in nature. AIMD was performed for 10 ps to prove the thermodynamic stability at room temperature, as shown in Supplemental Material [30], Fig. S4. Considering that Ag atoms can occupy different tetrahedral sites at a certain temperature, our calculations show that it is feasible to switch octahedral occupation to tetrahedral occupation by applying hydrostatic pressure, as shown in Fig. 1(c). Taking $AgBiS_2$ as an example, its tensile and compressive stresses are 3.56 and 4.71 GPa, respectively. In addition, compared with octahedral sites, tetrahedra occupied by silver atoms have lower free energy, which reveals that this type of AgBiX_2 with $R3m$ phase is stable.

Considering fourth-order anharmonicity, we calculate the anharmonic phonon dispersion at finite temperature [see Fig. 2(a)]. Detailed calculation methods are given in the Supplemental Material [30] (see also Refs. [35–39] therein). It can be seen that AgBiX_2 has no imaginary frequency, which means they are dynamically stable. For $AgBiS_2$ and $AgBiSe_2$, the low-lying phonon branches below 2 THz harden with increasing temperature due to the strong anharmonicity of Ag atoms. The higher optical phonons of $AgBiS_2$ remain unchanged with temperature, while $AgBiSe_2$ softens. $AgBiTe_2$ has only localized phonon modes that harden with temperature due to the presence of heavy atoms. Notably, there are several avoided crossing points (highlighted by black circles) between longitudinal acoustic (LA) phonon modes and low-frequency optical phonon modes along Γ-T, L-Γ, Γ-S, and F-Γ, which are signals of rattling modes [40,41], as depicted in Fig. 2(b). Figure 2(c) shows that this rattling vibration mode may originate from Bi and Ag atoms. The amplitude of Bi atoms in 1.363, 1.293, 1.444, and 0.565 THz is much larger than that of other atoms (see Figs. S5–S7), while the huge vibration modes in $AgBiSe_2$ and $AgBiTe_2$ originate from Ag atoms. The hybridization of acoustic and optical vibrations at the avoided-crossing point leads to strong anharmonicity in the solid. The coupling strength of the two phonon mode branches is determined by the gap at

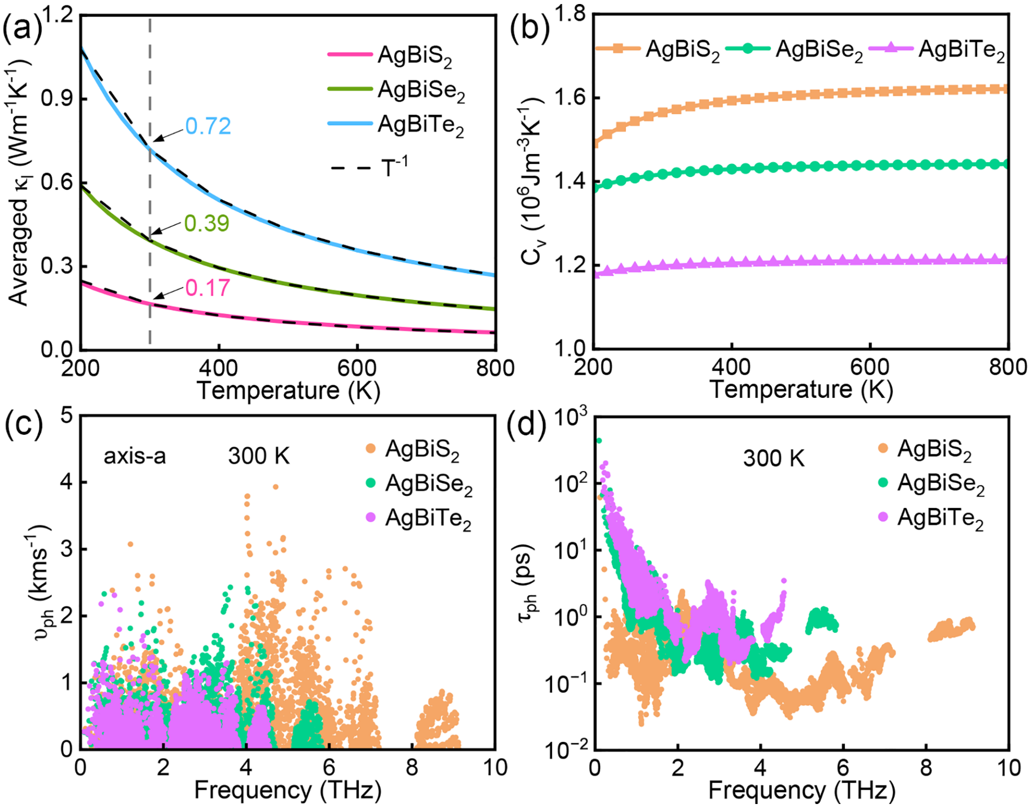

FIG. 3. Temperature-dependent (a) lattice thermal conductivity and (b) heat capacity, frequency-dependent (c) phonon group velocity and (d) phonon lifetime.

the avoided-crossing point. The phonon density of states (PhDOS) shows that Ag atoms in $AgBiS_2$ almost completely occupy the two TA phonon branches, while for $AgBiSe_2$ and $AgBiTe_2$, as the chalcogen atomic mass increases, the optical phonon branches are softened, which gradually overlap with TA phonon branches.

Atomic displacement parameters (ADPs) evaluate the mean-square displacement of atoms in a solid around its equilibrium position and reflect the strength of chemical bonds. The ADPs of Ag atoms along the in-plane direction (e.g., a axis) are larger than those of other atoms, indicating that they are weakly bound with adjacent atomic environment in the crystal lattice. In particular, the ADPs of Ag atoms in $AgBiS_2$ reaches 0.12 Å^2 at 300 K, which is significantly larger than that in $AgBiSe_2$ and $AgBiTe_2$. Such rattling atoms may induce low thermal conductivity due to the strong anharmonic vibrations [42].

B. Lattice thermal conductivity and phonon transport

The temperature dependence of κ_l calculated for $AgBiX_2$ from 200 to 800 K is shown in Fig. 3(a), which is the classical $\kappa_l \sim 1/T$ behavior in the framework of inherent three-phonon scattering mechanism. We found that $AgBiS_2$ has the lowest κ_l, contradicting the traditional Keyes theory [43] of the inverse relationship between κ_l and heavier elements. The lattice thermal conductivity in the phonon gas picture is calculated from the sum of all phonon modes as

$$\kappa_l = \sum_{\lambda} C_\lambda \nu_\lambda^2 \tau_\lambda, \tag{2}$$

where C, υ, and τ are the volume-heat capacity, group velocity, and phonon lifetime for the λ mode (composite index for the branch s and wave vector q), respectively. It is observed from Fig. 3(b) that the specific heat of $AgBiX_2$ increases with the increase of temperature, ranging from 1.1×10^{16} – 1.6×10^{16} $J/(m^3K)$. As the average atomic mass increases, the heat capacity and phonon group velocity [see Fig. 3(c)] decrease. According to the macroscopic elastic modulus [44], the transverse wave velocity (longitudinal wave velocity) of $AgBiS_2$, $AgBiSe_2$, and $AgBiTe_2$ are 3476.46 (1582.44), 3064.58 (1354.34), and 2826.85 (1284.83) m/s, respectively. There is a high group velocity of 3931 m/s near 4.71 THz for $AgBiS_2$ due to the presence of small-mass S atoms. For $AgBiS_2$ ($AgBiSe_2$ and $AgBiTe_2$), the average phonon group velocity is 431 m/s (299 and 241 m/s). Therefore, the phonon lifetime in Fig. 3(d) is direct evidence of the ultralow lattice thermal conductivity in $AgBiS_2$, and its phonon-scattering intensity far exceeds that of $AgBiSe_2$ and $AgBiTe_2$. From Fig. 3(d), the average phonon lifetime for $AgBiS_2$ ($AgBiSe_2$ and $AgBiTe_2$) is 0.32 ps (0.64 and 1.15 ps).

To further explain the ultralow κ_l of $AgBiS_2$, we calculated the decomposed phonon-scattering rate at room temperature, as shown in Fig. 4(a). The combination process of three-phonon scattering rates dominates at low frequency (below 1 THz), and gradually coexists with the splitting process between 2∼6 THz, while the splitting process prevails above 6 THz. There is a peak at 1 to 2 THz (see Fig. S8) due to the rattling mode of Bi atoms that causes the lowest optical branch to couple with the LA branch, thereby enhancing phonon-phonon scattering. It should be noted that this peak

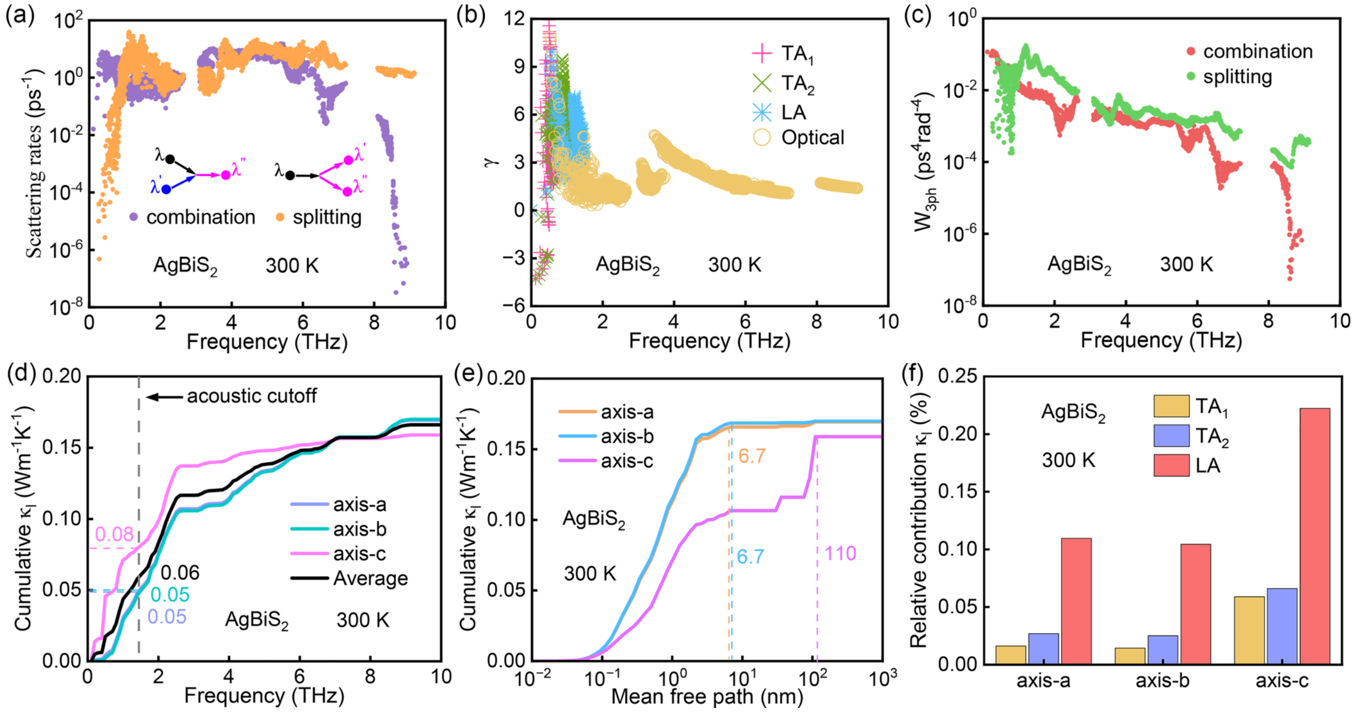

FIG. 4. (a) Decomposed anharmonic phonon-scattering rates for combination and splitting processes. (b) Grüneisen parameters for the acoustic and optical phonon branches. (c) Decomposed three-phonon weighted phase space for combining and splitting processes. (d) Frequency dependence of cumulative κ_l at 300 K. (e) Mean-free path dependence of κ_l integration. (f) Relative contribution of each acoustic branch to thermal conductivity.

also comes from the TA$_2$ branch, which is attributed to the strong anharmonic vibration of Ag atoms caused by the flat potential well. Some scattering rates exceed the phonon frequency, which means that specific phonon coherence is lost because the oscillation period is larger than its lifetime. The Grüneisen parameter (γ) and the weighted scattering phase space ($W_{3\mathrm{ph}}$) characterize the scattering intensity and the number of scattering channels, respectively, as shown in Figs. 4(b) and 4(c). The larger the absolute value of γ, the higher the anharmonicity. The average γ of AgBiS$_2$ is 2.78, which is much larger than AgBiSe$_2$ (1.91) and AgBiTe$_2$ (1.74). This reflects that the anharmonicity caused by Ag atoms gradually increases as the mass of the chalcogen element decreases in AgBiX_2. Figure 4(b) shows that the acoustic phonon mode has a larger γ compared with the optical phonon mode, and Ag atoms dominate the low-frequency anharmonicity in comparison to Bi atoms, as demonstrated by $\gamma_{\mathrm{TA}} > \gamma_{\mathrm{LA}}$. As depicted in Fig. 4(c), the scattering channel is almost dominated by splitting processes above 1 THz at room temperature.

In order to illustrate the thermal conduction process of phonon mode, we calculated the frequency cumulative κ_l at 300 K, as shown in Fig. 4(d). It can be clearly seen that the cumulative κ_l along the crystal axis gradually increases over the entire frequency range. The frequency range of 0∼1.4 THz has a significant contribution of 35% to κ_l, including acoustic and low-frequency optical branches [shown as the black line in Fig. 4(d)]. Therefore, the thermal conductivity contributed by optical phonons reaches above 65%, which exceeds the recently reported LaWN$_3$ (59%) [45] and LaWN$_3$ (60%) [46]. In addition, we plotted the cumulative κ_l versus phonon mean-free path (MFP) at 300 K. The maximum values of phonon MFP are 110 and 6.7 nm along the c- and a axes, respectively. The short MFP along axis a or axis b means that it is difficult to reduce the thermal conductivity through polycrystalline structures and nanostructures, while high-entropy alloying may be an effective way to modify the optical phonons with small MFP. Figure 4(f) clearly shows that the heat-carrying capacity of TA phonons is much lower than that of LA phonons, which is inverted with the Grüneisen trend, revealing that Ag atom-dominated TA phonons effectively suppress thermal conductivity.

C. Electrical transport and figures of merit

The electrical transport coefficient of a material depends largely on its electronic structure near the Fermi level. Figure 5(a) shows the electronic band structure of AgBiS$_2$, demonstrating an indirect band gap of ∼0.76 eV. The conduction-band minimum (CBM) is at point T; the valence-band maximum (VBM) and the secondary VBM (VBM2) are located at the Γ-S and L-Γ high-symmetry lines, respectively. The energy difference between VBM and VBM2 is very small (0.021 eV), which is smaller than that of PbTe (0.15 eV). The smaller energy difference indicates that both VBM and VBM2 could be beneficial to the electrical transport properties. AgBiSe$_2$ is also an indirect band (0.44 eV), but the positions of VBM and VBM2 are interchanged. For AgBiTe$_2$, there is a direct band gap of 0.36 eV at the T point. Likewise, there is only a slight energy difference between VBM and VBM2 in AgBiSe$_2$ and AgBiTe$_2$. In AgBiS$_2$, VBM mainly originates from Ag-d_{yz}, Bi-s, and S-p_y states, and CBM is contributed by Ag-s, Bi-p_x, and S-s states.

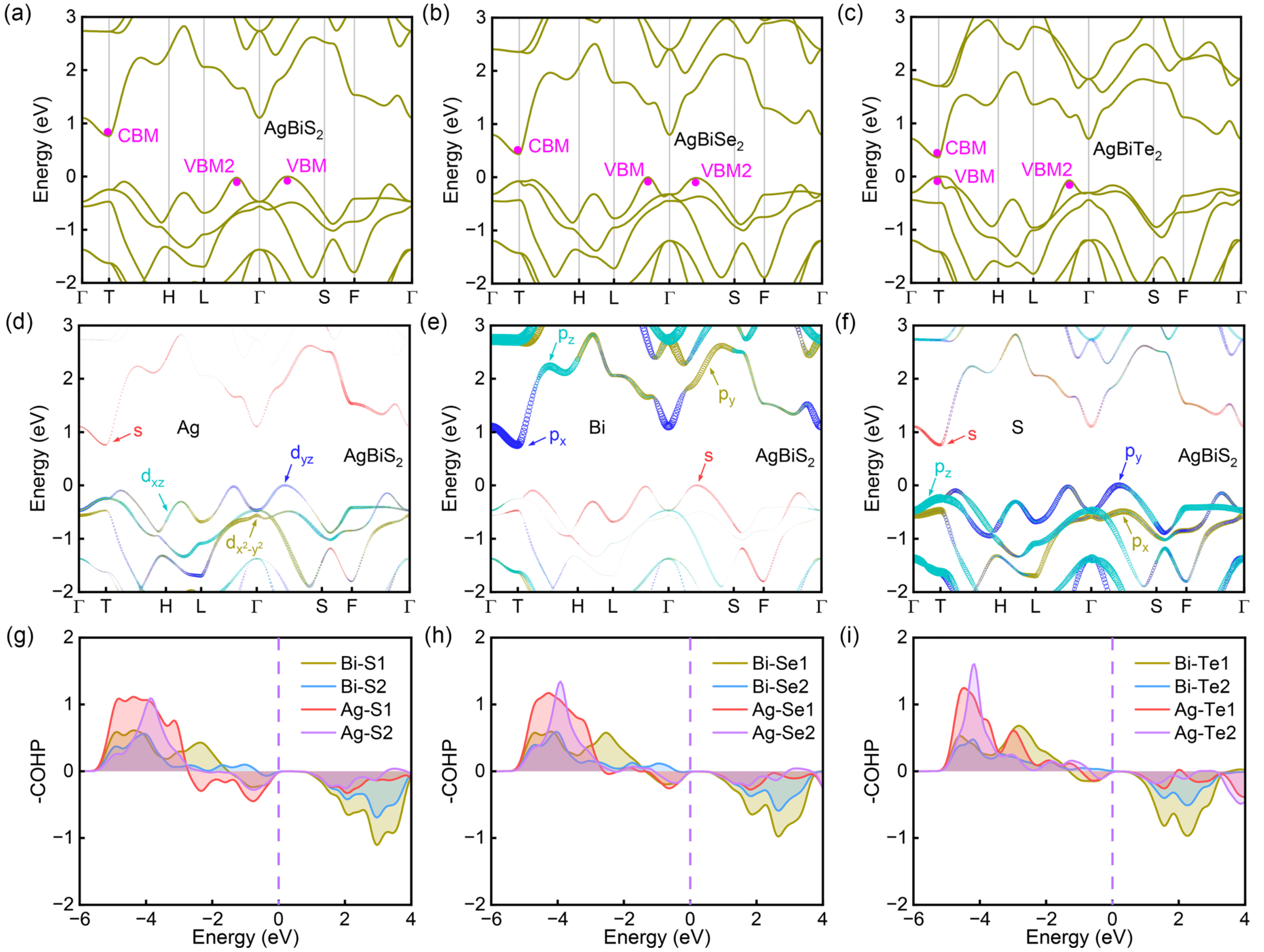

FIG. 5. (a)–(c) Band structure for AgBiX_2. (d)–(f) Orbital projection band structures of Ag atoms, Bi atoms, and S atoms in AgBiS$_2$. (g)–(i) The calculated crystal-orbital Hamilton population (COHP) analysis for AgBiX_2. The negative values of COHP present antibonding states. The Fermi energy level is set at 0 eV.

To further investigate the bonding characteristics of AgBiX_2 near the Fermi level, we calculated the crystal-orbital Hamilton population (COHP) using the LOBSTER package [47]. Positive- and negative-COHP values represent bonding and antibonding properties, respectively. The antibonding states at the bottom of the conduction band and the top of the valence band are mainly ionic bonds between metal atoms and sulfur atoms. As shown in Fig. 5(g), four bonds of AgBiS$_2$ participate in antibonding states near the Fermi level, more than AgBiSe$_2$ and AgBiTe$_2$, which directly proves that AgBiS$_2$ has giant anharmonicity. Figure S9 shows the integrated crystal-orbital Hamilton population of Ag-X and Bi-X (X = S, Se, or Te). As the chalcogen atomic number increases, the Ag–X bond strengthens, while the Bi–X bond first strengthens and then weakens. For the Ag–S1 and Bi–S1 bonds of AgBiS$_2$, the calculated integrated crystal-orbital bond index [48] is 0.5 and 0.6, respectively, while the Ag–S2 and Bi–S2 bonds are 0.37 and 0.35, which is close to that of PbTe (0.37), which is likely due to resonant bonding [49] and metavalent bonding [50]. This confirms the strong bond heterogeneity in the AgBiX_2 system.

Figure 6 shows the electron transport properties and thermoelectric figure of merit of p-type AgBiS$_2$. From Fig. 6(a), we find that $|S|$ decreases as the carrier concentration increases and increases as the temperature rises up, which is explained by Mott's formula [51], as

$$S = \frac{8\pi^2 k_B^2}{3eh^2} m^* T \left(\frac{\pi}{3n}\right)^{2/3}, \tag{3}$$

where k_B is the Boltzmann constant, e is the electron charge, h is the Plank constant, T is the temperature, and m^* is the density of states effective mass of carriers. In constrast, σ is directly proportional to the carrier concentration and inversely proportional to the temperature, which is consistent with the conductivity relationship in the Drude model [52], as

$$\sigma = \frac{ne^2}{m_c^*}\tau, \tag{4}$$

where m_c^* is the conductivity effective mass and τ is the electron relaxation time. The former is attributed to the dispersion of electronic bands near the Fermi level, while the latter reflects an increased scattering rate due to strong

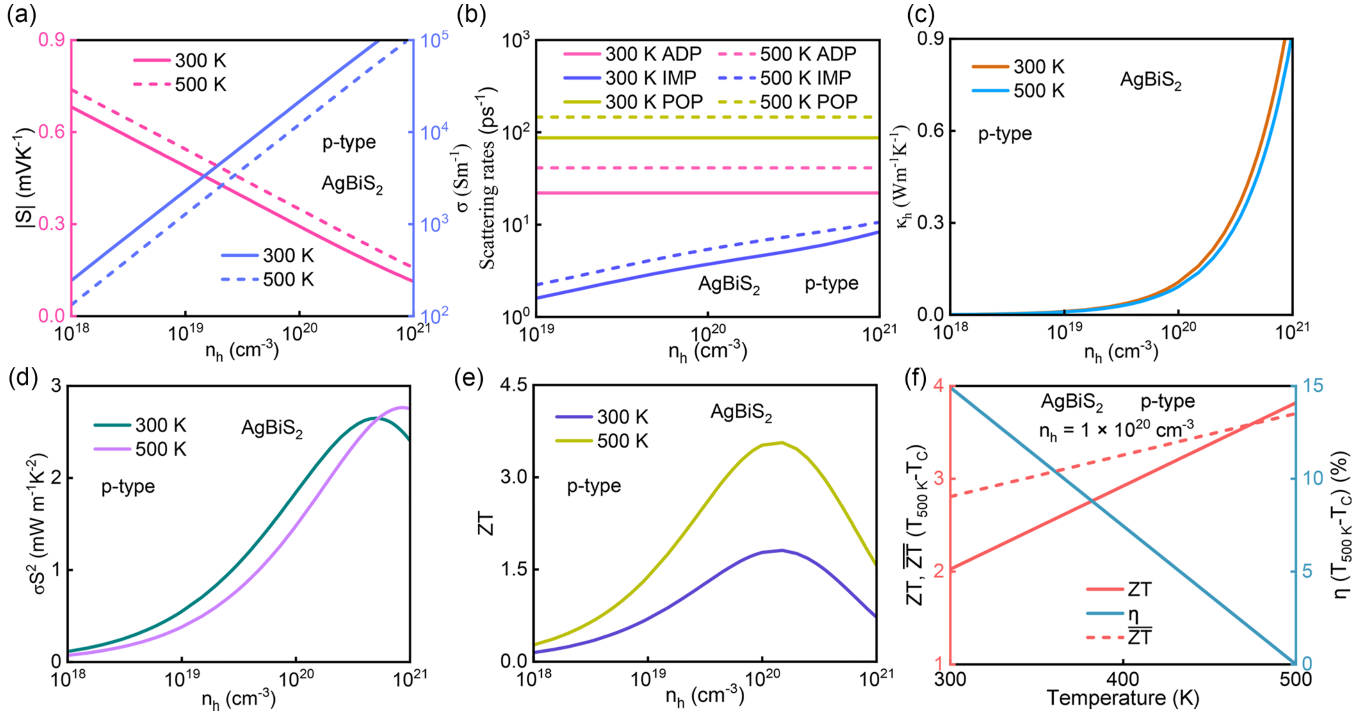

FIG. 6. Calculated electrical transport parameters and thermoelectric figure of merit for p-type AgBiS$_2$. (a) Seebeck coefficient |S| and conductivity σ. (b) Hole-scattering rates. (c) Electronic thermal conductivity κ_h. (d) Thermoelectric power factor. (e) Thermoelectric figure of merit. (f) Average thermoelectric figure of merit and conversion efficiency.

electron-phonon interactions caused by increasing temperature. The scattering process is mainly dominated by POP [see Fig. 6(b)], which also indicates that the rattling metal atoms contribute many low-frequency optical phonons. In general, κ_e and σ show the same trend determined by the Wiedemann-Franz law [52] as

$$\kappa_e = L\sigma T, \tag{5}$$

where L is the Lorentz constant. Due to the large |S| and high σ, a high-TE power factor is captured, reaching $2.48\,\mathrm{mW\,m^{-1}\,K^{-2}}$ for p-type AgBiS$_2$ at room temperature and optimal carrier concentration, as shown in Figs. 6(c) and 6(d). In addition, the spin-orbit coupling (SOC) effect caused by heavy elements in AgBiS$_2$ does not significantly change the electrical transport (see Fig. S10).

Combining extremely low κ_l with high-TE power factor, excellent TE performance is captured in this compound, as shown in Fig. 6(e). The highest ZT value for p-type AgBiS$_2$ reaches 1.77 (3.59) at $n_h \sim 1.5 \times 10^{20}\ \mathrm{cm^{-3}}$ at $T = 300$ (500) K. For n-type AgBiS$_2$, various electrical properties maintain a similar trend to that of p type as shown in Fig. S11, and ZT value reaches 1.32 at $n_e \sim 4 \times 10^{18}\ \mathrm{cm^{-3}}$ under $T = 500$ K. We evaluated the conversion efficiency (η) of AgBiS$_2$-based thermoelectric devices based on the following formula:

$$\eta = \frac{T_h - T_c}{T_h} \frac{\sqrt{\overline{ZT}+1}-1}{\sqrt{\overline{ZT}+1}+T_c/T_h}, \tag{6}$$

which depends on the average ZT, i.e., $\overline{ZT} = \frac{1}{T_h - T_c}\int_{T_c}^{T_h} ZT\,dT$, where T_c and T_h represent the temperatures of the cold and hot sides of the thermoelectric device, respectively. In Fig. 6(f), it can be seen that the maximum η is as high as 15% in the temperature range of 200–500 K, approaching the recently reported 15.5% of PbTe [53]. Figure S12 shows that the highest ZT value of p-type AgBiSe$_2$ (AgBiTe$_2$) reaches 1.13 (1.15) at $n_h \sim 9 \times 10^{19}\ \mathrm{cm^{-3}}$ ($\sim 8.5 \times 10^{19}\ \mathrm{cm^{-3}}$).

As shown in Fig. 7(a), ZT value gradually increases under isotropic tensile stress and decreases under compressive stress in the strain engineering. Surprisingly, ZT value reaches 2.6 by tensile stress of 0.75% at carrier concentration of $1 \times 10^{20}\ \mathrm{cm^{-3}}$ under room temperature. Figure 7(b) and Fig. S13 show that under isotropic tensile stress, the electrical transport properties only slightly change, while the thermal conductivity decreases significantly. Figure S14 shows that the decrease in thermal conductivity is mainly attributed to the decrement of phonon lifetime, particularly at low-frequency branch. From the phonon dispersion, one can see that lattice vibrations harden under compressive stress while softening under tensile stress. Interestingly, phonons at M1, M2, and M3 are significantly softened under tensile stress, demonstrating very small vibration frequency of ∼0.087 THz. Figure 7(d) reveals that these phonons mainly come from intercalated Ag atoms that exhibit large vibration amplitudes. The softened phonon branches remarkably prompt the three-phonon scattering process which suppresses thermal transport during tensile strain. In summary, tensile strain clearly suppresses thermal transport in AgBiS$_2$: (i) strong anharmonicity caused by weak bonding, (ii) softened phonon branches significantly promote three-phonon scattering, and (iii) partial phonon gas picture failure [54–56]. This suggests that strain engineering is helpful for reducing lattice thermal conductivity.

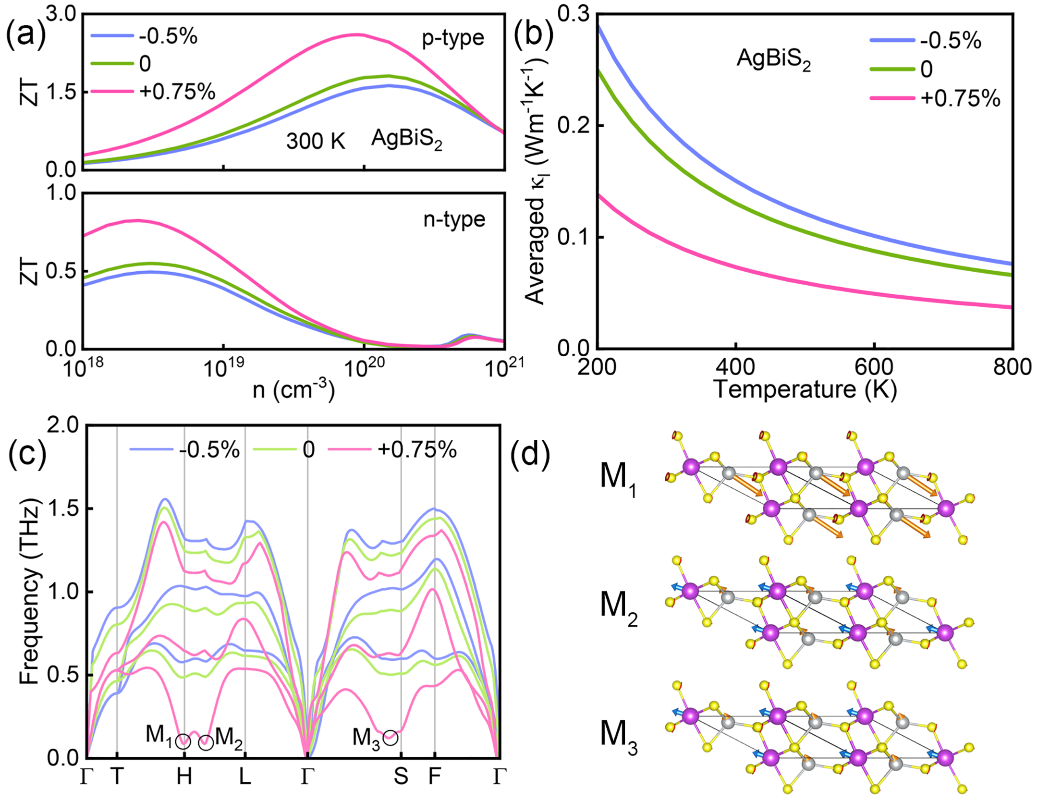

FIG. 7. Thermoelectric properties of $AgBiS_2$ in strain. (a) Thermoelectric figure of merit in strain. (b) Lattice thermal conductivity of $AgBiS_2$ in strain. (c) Acoustic-branch phonon dispersion of $AgBiS_2$ in strain. (d) Atomic vibration modes of $AgBiS_2$ under stretching. The plus and minus signs represent tensile and compressive stress, respectively.

IV. CONCLUSION

In summary, the thermal transport and electrical transport properties of Ag-based intercalated layered materials were studied using the first-principles calculation combined with the Boltzmann transport equation. The ultralow thermal conductivity of $AgBiX_2$ was ascribed to the strong phonon scattering caused by the rattling mode which was induced by metal atoms. As the atomic number of chalcogen increased, lattice thermal conductivity of $AgBiX_2$ decreased due to the enhanced anharmonicity of Ag atoms. It was found that the thermal conductivity of $AgBiS_2$ was mainly dominated by optical phonon modes, which was attributed to the strong anharmonicity of Ag atoms and suppression of TA heat-carrying phonons. Considering the ADP, POP, and IMP scattering mechanisms, *p*-type $AgBiS_2$ was predicted to be an excellent thermoelectric material at room temperature, and its *ZT* value could be further improved through moderate strain engineering. The present work shows that the class of Ag-based intercalated layered compounds are promising thermoelectric candidates for potential applications.

ACKNOWLEDGMENTS

This work was supported by National Natural Science Foundation of China (Grants No. 12174450 and No. 11874429), National Talents Program of China, Hunan Provincial Key Project No. 2024JJ3029, Key Research and Development Program (Grant No. 2022WK2002), Distinguished Youth Foundation (Grant No. 2020JJ2039), Project of High-Level Talents Accumulation (Grant No. 2018RS3021), Program of Hundreds of Talents, State Key Laboratory of Powder Metallurgy, Start-up Funding and Innovation-Driven Plan (Grant No. 2019CX023) of Central South University, and Postgraduate Scientific Research Innovation Project of Hunan Province (Grants No. CX20230104 and No. CX20220252). Calculations were performed at High-Performance Computing facilities of Central South University.

---

[1] L. Su, D. Wang, S. Wang, B. Qin, Y. Wang, Y. Qin, Y. Jin, C. Chang, and L.-D. Zhao, High thermoelectric performance realized through manipulating layered phonon-electron decoupling, Science **375**, 1385 (2022).

[2] C. Zhou, Y. K. Lee, Y. Yu, S. Byun, Z.-Z. Luo, H. Lee, B. Ge, Y.-L. Lee, X. Chen, J. Y. Lee, O. Cojocaru-Mirédin, H. Chang, J. Im, S.-P. Cho, M. Wuttig, V. P. Dravid, M. G. Kanatzidis, and I. Chung, Polycrystalline SnSe with a thermoelectric figure of merit greater than the single crystal, Nat. Mater. **20**, 1378 (2021).

[3] K. Biswas, J. He, I. D. Blum, C.-I. Wu, T. P. Hogan, D. N. Seidman, V. P. Dravid, and M. G. Kanatzidis,

High-performance bulk thermoelectrics with all-scale hierarchical architectures, Nature (London) **489**, 414 (2012).

[4] L.-D. Zhao, C. Chang, G. Tan, and M. G. Kanatzidis, SnSe: A remarkable new thermoelectric material, Energy Environ. Sci. **9**, 3044 (2016).

[5] B. Li, H. Wang, Y. Kawakita, Q. Zhang, M. Feygenson, H. L. Yu, D. Wu, K. Ohara, T. Kikuchi, K. Shibata, T. Yamada, X. K. Ning, Y. Chen, J. Q. He, D. Vaknin, R. Q. Wu, K. Nakajima, and M. G. Kanatzidis, Liquid-like thermal conduction in intercalated layered crystalline solids, Nat. Mater. **17**, 226 (2018).

[6] H. Liu, X. Shi, F. Xu, L. Zhang, W. Zhang, L. Chen, Q. Li, C. Uher, T. Day, and G. J. Snyder, Copper ion liquid-like thermoelectrics, Nat. Mater. **11**, 422 (2012).

[7] J. Yang, W. Zhang, S. Q. Bai, Z. Mei, and L. D. Chen, Dual-frequency resonant phonon scattering in $Ba_xR_yCo_4Sb_{12}$ (R = La, Ce, and Sr), Appl. Phys. Lett. **90**, 192111 (2007).

[8] C. Chang, M. Wu, D. He, Y. Pei, C.-F. Wu, X. Wu, H. Yu, F. Zhu, K. Wang, Y. Chen, L. Huang, J.-F. Li, J. He, and L.-D. Zhao, 3D charge and 2D phonon transports leading to high out-of-plane ZT in n-type SnSe crystals, Science **360**, 778 (2018).

[9] S. Roychowdhury, T. Ghosh, R. Arora, U. V. Waghmare, and K. Biswas, Stabilizing n-type cubic GeSe by entropy-driven alloying of $AgBiSe_2$: Ultralow thermal conductivity and promising thermoelectric performance, Angew. Chem. Int. Ed. **57**, 15167 (2018).

[10] L. Cheng, J. Yuan, M. Yao, M. Li, and H. Wang, Giant thermoelectric effect in rare earth sulfoiodides, J. Phys. Chem. C **127**, 20572 (2023).

[11] A. Bhui, S. Das, R. Arora, U. Bhat, P. Dutta, T. Ghosh, R. Pathak, R. Datta, U. V. Waghmare, and K. Biswas, Hg doping induced reduction in structural disorder enhances the thermoelectric performance in $AgSbTe_2$, J. Am. Chem. Soc. **145**, 25392 (2023).

[12] T. Ghosh, M. Dutta, D. Sarkar, and K. Biswas, Insights into low thermal conductivity in inorganic materials for thermoelectrics, J. Am. Chem. Soc. **144**, 10099 (2022).

[13] S. Roychowdhury, T. Ghosh, R. Arora, M. Samanta, L. Xie, N. K. Singh, A. Soni, J. He, U. V. Waghmare, and K. Biswas, Enhanced atomic ordering leads to high thermoelectric performance in $AgSbTe_2$, Science **371**, 722 (2021).

[14] J. L. Niedziela, D. Bansal, A. F. May, J. Ding, T. Lanigan-Atkins, G. Ehlers, D. L. Abernathy, A. Said, and O. Delaire, Selective breakdown of phonon quasiparticles across superionic transition in $CuCrSe_2$, Nat. Phys. **15**, 73 (2019).

[15] F. Gascoin and A. Maignan, Order–disorder transition in $AgCrSe_2$: A new route to efficient thermoelectrics, Chem. Mater. **23**, 2510 (2011).

[16] A. M. Ganose, J. Park, A. Faghaninia, R. Woods-Robinson, K. A. Persson, and A. Jain, Efficient calculation of carrier scattering rates from first principles, Nat. Commun. **12**, 2222 (2021).

[17] G. Kresse and J. Furthmüller, Efficient iterative schemes for ab initio total-energy calculations using a plane-wave basis set, Phys. Rev. B **54**, 11169 (1996).

[18] P. E. Blöchl, Projector augmented-wave method, Phys. Rev. B **50**, 17953 (1994).

[19] J. P. Perdew, K. Burke, and M. Ernzerhof, Generalized gradient approximation made simple, Phys. Rev. Lett. **77**, 3865 (1996).

[20] W. Xie, X. Xu, M. Li, and H. Wang, Intrinsic Rashba effect and anomalous valley Hall effect in one-dimensional magnetic nanoribbon, J. Magn. Magn. Mater. **573**, 170662 (2023).

[21] P. Zuo, H. Wang, Z. Wang, and R. Wu, Large magnetic anisotropy of single transition metal adatoms on WS_2, J. Magn. Magn. Mater. **506**, 166796 (2020).

[22] W. Xie, L. Zhang, Y. Yue, M. Li, and H. Wang, Giant valley polarization and perpendicular magnetocrystalline anisotropy energy in monolayer MX_2(M = Ru, Os; X = Cl, Br), Phys. Rev. B **109**, 024406 (2024).

[23] Z. Yang, M. Yao, J. Pan, L. Huang, M. Li, and H. Wang, Large magnetostriction of heavy-metal-element doped Fe-based alloys, J. Appl. Phys. **132**, 215105 (2022).

[24] A. Togo and I. Tanaka, First principles phonon calculations in materials science, Scr. Mater. **108**, 1 (2015).

[25] W. Li, J. Carrete, N. A. Katcho, and N. Mingo, ShengBTE: A solver of the Boltzmann transport equation for phonons, Comput. Phys. Commun. **185**, 1747 (2014).

[26] Z. Zhang, X. Jiang, T. Hattori, X. Xu, M. Li, C. Yu, Z. Zhang, D. Yu, R. Mole, S. Yano, J. Chen, L. He, C.-W. Wang, H. Wang, B. Li, and Z. Zhang, A colossal barocaloric effect induced by the creation of a high-pressure phase, Mater. Horiz. **10**, 977 (2023).

[27] W. Li, L. Lindsay, D. A. Broido, D. A. Stewart, and N. Mingo, Thermal conductivity of bulk and nanowire $Mg_2Si_xSn_{1-x}$ alloys from first principles, Phys. Rev. B **86**, 174307 (2012).

[28] X. Xu, F. Li, C. Niu, M. Li, and H. Wang, Machine learning assisted investigation of the barocaloric performance in ammonium iodide, Appl. Phys. Lett. **122**, 043901 (2023).

[29] F. Li, M. Li, C. Niu, and H. Wang, Atomic-scale insights into the colossal barocaloric effects of neopentyl glycol plastic crystals, Appl. Phys. Lett. **120**, 073902 (2022).

[30] See Supplemental Material at http://link.aps.org/supplemental/10.1103/PhysRevB.109.235202 for the crystal structure, potential energy, electron locational fuction, thermodynamic stability, mechanical parameters, electrical transport parameters, atomic vibration modes, phonon-scattering rate, integrated crystal-orbital Hamilton population, integrated crystal-orbital bond index, thermoelectric figure of merit, electrical transport properties with SOC, electrical transport properties, and phonon parameters under stress.

[31] T. Gürel, Y. A. Altunay, P. Bulut, S. Yıldırım, and C. Sevik, Comprehensive investigation of the extremely low lattice thermal conductivity and thermoelectric properties of $BaIn_2Te_4$, Phys. Rev. B **106**, 195204 (2022).

[32] K. Koumpouras and J. A. Larsson, Distinguishing between chemical bonding and physical binding using electron localization function (ELF), J. Phys. Condens. Matter **32**, 315502 (2020).

[33] F. Mouhat and F.-X. Coudert, Necessary and sufficient elastic stability conditions in various crystal systems, Phys. Rev. B **90**, 224104 (2014).

[34] M. Hu, C. Ge, J. Yu, and J. Feng, Mechanical and optical properties of Cs_4BX_6(B = Pb, Sn; X = Cl, Br, I) zero-dimension perovskites, J. Phys. Chem. C **121**, 27053 (2017).

[35] F. Zhou, W. Nielson, Y. Xia, and V. Ozoliņš, Lattice anharmonicity and thermal conductivity from compressive sensing of first-principles calculations, Phys. Rev. Lett. **113**, 185501 (2014).

[36] T. Tadano and S. Tsuneyuki, First-principles lattice dynamics method for strongly anharmonic crystals, J. Phys. Soc. Jpn. **87**, 041015 (2018).

[37] H. Zou, The adaptive lasso and its oracle properties, J. Am. Stat. Assoc. **101**, 1418 (2006).

[38] T. Tadano and S. Tsuneyuki, Self-consistent phonon calculations of lattice dynamical properties in cubic $SrTiO_3$ with first-principles anharmonic force constants, Phys. Rev. B **92**, 054301 (2015).

[39] T. Tadano, Y. Gohda, and S. Tsuneyuki, Anharmonic force constants extracted from first-principles molecular dynamics: Applications to heat transfer simulations, J. Phys.: Condens. Matter **26**, 225402 (2014).

[40] S. Han, S. Dai, J. Ma, Q. Ren, C. Hu, Z. Gao, M. Duc Le, D. Sheptyakov, P. Miao, S. Torii, T. Kamiyama, C. Felser, J. Yang, C. Fu, and T. Zhu, Strong phonon softening and avoided crossing in aliovalence-doped heavy-band thermoelectrics, Nat. Phys. **19**, 1649 (2023).

[41] M. Christensen, A. B. Abrahamsen, N. B. Christensen, F. Juranyi, N. H. Andersen, K. Lefmann, J. Andreasson, C. R. H. Bahl, and B. B. Iversen, Avoided crossing of rattler modes in thermoelectric materials, Nat. Mater. **7**, 811 (2008).

[42] C. Chang and L.-D. Zhao, Anharmoncity and low thermal conductivity in thermoelectrics, Mater. Today Phys. **4**, 50 (2018).

[43] R. W. Keyes, High-temperature thermal conductivity of insulating crystals: Relationship to the melting point, Phys. Rev. **115**, 564 (1959).

[44] O. L. Anderson, A simplified method for calculating the Debye temperature from elastic constants, J. Phys. Chem. Solids **24**, 909 (1963).

[45] Q. Ren, Y. Li, Y. Lun, G. Tang, and J. Hong, First-principles study of the lattice thermal conductivity of the nitride perovskite $LaWN_3$, Phys. Rev. B **107**, 125206 (2023).

[46] M. Jian, Z. Feng, Y. Xu, Y. Yan, G. Zhao, and D. J. Singh, Ultralow lattice thermal conductivity induced by anharmonic cation rattling and significant role of intrinsic point defects in $TlBiS_2$, Phys. Rev. B **107**, 245201 (2023).

[47] R. Nelson, C. Ertural, J. George, V. L. Deringer, G. Hautier, and R. Dronskowski, LOBSTER: Local orbital projections, atomic charges, and chemical-bonding analysis from projector-augmented-wave-based density-functional theory, J. Comput. Chem. **41**, 1931 (2020).

[48] P. C. Müller, C. Ertural, J. Hempelmann, and R. Dronskowski, Crystal orbital bond index: Covalent bond orders in solids, J. Phys. Chem. C **125**, 7959 (2021).

[49] S. Lee, K. Esfarjani, T. Luo, J. Zhou, Z. Tian, and G. Chen, Resonant bonding leads to low lattice thermal conductivity, Nat. Commun. **5**, 3525 (2014).

[50] J. Raty, M. Schumacher, P. Golub, V. L. Deringer, C. Gatti, and M. Wuttig, A quantum-mechanical map for bonding and properties in solids, Adv. Mater. **31**, 1806280 (2019).

[51] M. Cutler, J. F. Leavy, and R. L. Fitzpatrick, Electronic transport in semimetallic cerium sulfide, Phys. Rev. **133**, A1143 (1964).

[52] G. Tan, L.-D. Zhao, and M. G. Kanatzidis, Rationally designing high-performance bulk thermoelectric materials, Chem. Rev. **116**, 12123 (2016).

[53] B. Jia, D. Wu, L. Xie, W. Wang, T. Yu, S. Li, Y. Wang, Y. Xu, B. Jiang, Z. Chen, Y. Weng, and J. He, Pseudo-nanostructure and trapped-hole release induce high thermoelectric performance in PbTe, Science **384**, 81 (2024).

[54] S. Tang, S. Bai, M. Wu, D. Luo, J. Zhang, D. Wang, S. Yang, and L.-D. Zhao, Improving thermoelectric performance of asymmetrical Janus 1T-SnSSe monolayer by the synergistic effect of band convergence and crystal lattice softening under strain engineering, Mater. Today Phys. **29**, 100923 (2022).

[55] A. Kundu, Y. Chen, X. Yang, F. Meng, J. Carrete, M. Kabir, G. K. H. Madsen, and W. Li, Electron-induced nonmonotonic pressure dependence of the lattice thermal conductivity of θ-TaN, Phys. Rev. Lett. **132**, 116301 (2024).

[56] M. Simoncelli, N. Marzari, and F. Mauri, Unified theory of thermal transport in crystals and glasses, Nat. Phys. **15**, 809 (2019).